A Robust Resonant Controller for High-Speed Scanning of Nanopositioners: Design and Implementation

Jie Ling, Micky Rakotondrabe, *Member, IEEE*, Zhao Feng, Min Ming, and Xiaohui Xiao, *Member, IEEE*

***Abstract*— This brief presents a novel damping control scheme for piezoactuated nanopositioning platforms with robust resonant control (RRC). The RRC is developed to attenuate the resonant-vibrational modes of the lightly damped dynamics of the stage in an inner positive feedback loop. The parameters in the proposed RRC are determined through an analytical approach. Indeed, the controller gains constrained by both the robustness and the damping ratio of the inner loop are tuned based on the small gain theory. Then, a high gain integral tracking controller is applied in the outer loop to minimize the tracking errors due to unmodeled nonlinearity and uncertainties. To validate the effectiveness of the proposed RRC, comparative experiments with conventional positive position feedback (PPF) and integral resonant control (IRC) are conducted on a piezoactuated nanopositioning stage. Results demonstrate that the proposed RRC improves the closed-loop bandwidth from 67 Hz with PPF and 135 Hz with IRC to 176 Hz. Moreover, better robustness against load variations with a range of 0–1000-g loading under 0–20-Hz input raster scanning signals are obtained by RRC compared with PPF as well as IRC.**

***Index Terms*— High-speed scanning, piezoelectric nanopositioner, resonant control (RC), robustness.**

I. Introduction

NANOPOSITIONERS have been widely used in high-precision positioning applications, including, but not limited to, microrobotics, microassembly, microlithography, micromanipulation, microfabrication, and microscopy scanning [1]–[3]. Because of the merits of fast dynamics, large output forces, and subnanometer resolution, piezoelectric ceramics are commonly applied to actuate these nanopositioners [4]. Unfortunately, the operating bandwidth of a piezoactuated nanopositioner is usually limited to 10–100 times lower than the lowest resonant frequency because of its lightly damped resonant-vibrational modes [5], [6].

Manuscript received October 12, 2018; revised January 28, 2019; accepted February 11, 2019. Date of publication March 4, 2019; date of current version April 13, 2020. Manuscript received in final form February 11, 2019. This work was supported in part by the Shenzhen Science and Technology Program under Grant JCYJ20170306171514468, in part by the National Natural Science Foundation of China under Grant 51375349, and in part by the China Postdoctoral Science Foundation under Grant 2018M642905. Recommended by Associate Editor S. Pirozzi. *(Corresponding author: Xiaohui Xiao.)*

J. Ling, Z. Feng, and M. Ming are with the Hubei Key Laboratory of Waterjet Theory and New Technology, Wuhan University, Wuhan 430072, China (e-mail: jamesling@whu.edu.cn; fengzhaozhao7@whu.edu.cn; mingmin_whu@whu.edu.cn).

M. Rakotondrabe is with the FEMTO-ST Institute, Universit Bourgogne Franche-Comt/ENSMM/CNRS, 25000 Besançon, France (e-mail: mrakoton@femto-st.fr).

X. Xiao is with the Hubei Key Laboratory of Waterjet Theory and New Technology, Wuhan University, Wuhan 430072, China, and also with the Shenzhen Institute, Wuhan University, Shenzhen 518057, China (e-mail: xhxiao@whu.edu.cn).

Color versions of one or more of the figures in this article are available online at http://ieeexplore.ieee.org.

Digital Object Identifier 10.1109/TCST.2019.2899566

Different control approaches have been raised for damping the resonant modes and high-bandwidth tracking of piezoactuated nanopositioners [7]. Among them, feedback architectures are most widely used for the superiority of robustness against external disturbances and model uncertainties [8]. Some general strategies are reported in the literature to minimize the tracking errors during the processes of high-speed tasks, such as H_∞ control [9], adaptive control [10], linear quadratic Gaussian control [11], and so on. These approaches permitted to find the controllers that ensured robust performance when the Q-factor of the system was low. Conversely, once the Q-factor becomes large and the system presents a very light damping ratio, the finding of a controller that ensures high damping performance becomes difficult with these approaches [9]. Hence, other specific model-based strategies for piezonanopositioners were developed with prioritized focus on damping control. These include: recursive-delayed position feedback [5], robust mass damper [12], and model reference control [13].

In addition to the above-mentioned works, negative-imaginary control is a class of control approaches that are applicable to deal with problems of resonant vibrations of flexible structures with lightly damped modes [14], [15]. The negative imaginary theory provides a solution to increase damping of the vibrational modes as well as to maintain the robustness against modal uncertainty and unmodeled dynamics simultaneously [15]. A number of well-performing damping controllers based on negative-imaginary theory have then been developed to damp resonant modes but also to increase the bandwidth of the piezonanopostioners. These efforts include: passive shunt-damping [13], positive position feedback (PPF) [16], positive velocity and position feedback [17], resonant control (RC) [18], integral RC (IRC) [19], [20], and so on. All the imaginary controllers mentioned above have fixed structures with low order and low computational complexity, which makes them simple in the design and implementation. Moreover, when implementing the control laws using digital signal processing equipment, the property of fixed structure and low order allows for the highest possible sampling frequency [13]. However, apart from the IRC and the integral force feedback (IFF) approaches, a primary drawback of the other controllers lies in that these controllers are designed to damp each resonant mode separately. For a system with only one dominant mode (generally the first resonant mode), these controllers can be applicable with low order. However, for a system with multimode resonant frequencies, these controllers will lead to high order, which is not practical to implement [20]. Different from IFF, which needs additional sensors, IRC is more flexible. Therefore, among the aforementioned

approaches, IRC is the most applicable damping approach for both systems with unique vibrational mode and with multiresonant modes.

In a general IRC design, a feedthrough term is added to induce a new pair of resonant zeros at a frequency below the first resonant mode. A simple integrator is then applied in the positive feedback loop to damp the vibrational modes. With the increasing controller gain, poles of the closed loop will move away from the imaginary until the damping ratio reaches a peak point [19], [20]. As these two parameters (feedthrough term and controller gain) in the IRC scheme can be calculated and determined analytically if the transfer function of the nominal system is identified as demonstrated in [20], it is simple and practical for users to design and implement the controller. However, for piezoactuated nanopositioners applied on those occasions, where the variation of loaded mass or environmental temperature leads to significant changes in nominal resonant frequency, the standard IRC designed on the basis of the nominal system may result in unsatisfied performance against uncertainty. Inspired by the efforts for standard IRC in [19] and [20], a novel robust resonant controller (RRC) consisting of a feedthrough term and a second-order damping controller is proposed in this brief.

The contributions of this brief are threefold. First, a second-order damping controller is integrated with a feedthrough term to synthesize a novel RRC. It should be noted that the second-order damping controller in the proposed RRC is referred from PPF [16] for its high robustness against uncertainty. For this, the proposed RRC structure as well as its objective is totally different from the existing bandpass filter in IRC scheme, which is also a second-order damper. Second, the analytical relationship between controller parameters is derived. Then, a tradeoff between closed-loop bandwidth and damping ratio based on the small-gain theory is proposed for controller design. Third, an illustrative example with a piezoactuated nanopositioner accompanied by experiments and discussions is presented. The robustness of the proposed RRC is studied by simulations and experiments. Comparison with existing PPF and IRC schemes under different load variations on the platform is also conducted.

The rest of this brief is organized as follows. The existing standard IRC scheme is reviewed in Section II. Then, Section III describes the design of the proposed RRC. The experimental setup and the system identification are presented in Section IV. Verifications and discussions are given in Section V. Finally, Section VI concludes this brief.

II. Conventional IRC Scheme

Assuming a piezoactuated nanopositioner with a lightly damped mode, the dominant dynamics can be approximately identified as a second-order system as

$$G(s) = \frac{\sigma^2}{s^2 + 2\xi_n\omega_n \cdot s + \omega_n^2} \tag{1}$$

where s is the Laplace operator for continuous system, σ^2 is the gain of this resonant mode, ξ_n is the damping coefficient, and ω_n is the natural frequency. In this system, $\xi_n \ll 1$, which indicates that the resonant mode around the frequency of ω_n is lightly damped.

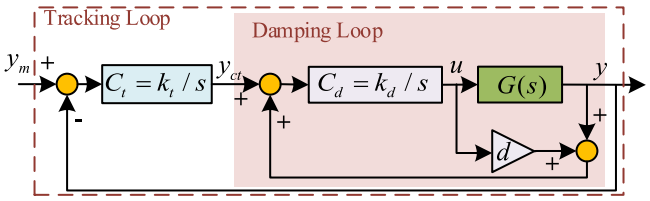

Fig. 1. Conventional IRC scheme.

Fig. 1 shows the conventional IRC scheme, where G is the identified model, C_d is the damping controller, C_t is the tracking controller, d is a feedthrough term, and y_m, y_{ct}, and y are the input references, tracking controller output, and closed-loop output, respectively. Here, the inner loop from y_m to y is denoted as the damping loop with a transfer function as

$$T_{\text{damp}}(s) \triangleq \frac{C_d(s) \cdot G(s)}{1 - C_d(s) \cdot (G(s) + d)}. \tag{2}$$

The damping controller gain k_d is found to maximize the damping ratio of the damping loop, which can be calculated by

$$k_d|_{\xi_{\max}} = \frac{1}{|d|}\left(\omega_n \cdot \sqrt{\frac{\omega_n}{\omega_n^2 + \sigma^2/d}}\right) \tag{3}$$

where $\xi_{\max}$ is the achievable maximum damping ratio; the feedthrough term can be chosen as $d = -2\sigma^2/\omega_n^2$.

For the tracking controller design, the gain should obey the following inequality:

$$k_t \cdot k_d < -\frac{\sigma^2 + d \cdot \omega_n^2}{d^2}. \tag{4}$$

It is notable that only the inner damping loop in (2) is related to damp the resonant-vibrational mode of (1). The tracking controller in external loop is used to minimize tracking errors, especially in the low-frequency region.

For conventional IRC parameters' selection and tuning, the model uncertainty resulted from load variation or surrounding environmental change is considered neither in the original design approach [19] nor in the improved analytical design approach [20]. Therefore, the robustness against uncertainty of the conventional IRC needs to be improved, which will be experimentally verified in Section V.

III. Proposed Robust Resonant Control Scheme

In this section, a new control scheme named RRC is suggested. In addition, the design process for parameters in the RRC is discussed analytically.

As depicted in Fig. 2, inspired by PPF control and IRC control, we propose a robust second-order controller in the inner damping loop to replace the simple integral damper in the conventional IRC. In the outer loop, a commonly used tracking controller is applied to eliminate tracking errors. Parameters in the damping controller will be discussed through an analytical approach, and the controller gains will be tuned based on the small-gain theory in Sections III-A and III-B.

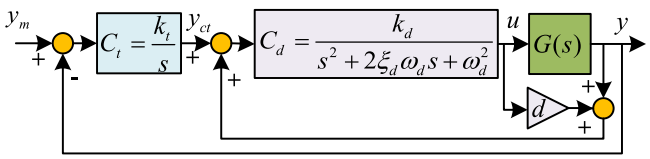

Fig. 2. Proposed RRC scheme.

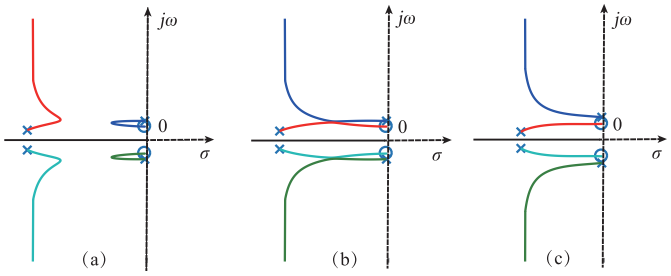

Fig. 3. Root locus of the damping loop with RRC. (a) Trajectory of resonant mode starts from the natural poles and ends at induced zeros by the feedthrough term (*Ordered state*). (b) Trajectories have a pair of complex breakaway points (*Critical state*). (c) Trajectories start from the natural poles and do not end on induced zeros (*Chaotic state*).

A. Parameter Selection

1) Feedthrough Term d: The purpose of adding a feedthrough term is to induce a pair of zeros in the root locus of the damping loop in (2). With the increasing controller gain, the root locus will start from the natural poles and end at the added resonant zeros, where a maximum damping ratio can always be found for the resonant mode. Furthermore, for a collocated system with multiresonant modes, e.g., a piezoelectric cantilever beam, the adding of a feedthrough term results in compound dynamics with interlaced zeros than poles. Then, all the resonant modes can be damped consistently when tuning controller gain. This is well explained and analyzed in [20]. In the RRC scheme, the feedthrough term is chosen as the same with IRC as $d = -2\sigma^2/\omega_n^2$.

2) ω_d and ξ_d: Considering the damping loop in (2) by replacing the damping controller with a second-order damper shown in Fig. 2, there are four poles with two from the natural system and the other two resulted from the damping controller, and two zeros induced from the added feedthrough term. For this, the root locus of the damping loop will have four trajectories, among which four trajectories start from the four poles, while two trajectories end at the induced zeros and two trajectories end at infinity. Fig. 3 displays the three possible cases of the root locus of the damping loop with different values of the two parameters (i.e., ω_d and ξ_d). The three states are named *"Ordered", "Critical," and "Chaotic"*, respectively. To damp the multiresonant modes of a collocated system simultaneously and consistently, the root locus of the damping loop needs to follow the ordered trajectories as shown in Fig. 3(a), which means that all the resonant modes start from the natural poles and end at the induced zeros, while the two roots induced by the damping controller move to infinite points.

For this, the proper range for ω_d and ξ_d needs to be found so that the resulted root locus of the damping loop would follow the ordered trajectories. Considering the critical state shown in Fig. 3(b), there is a pair of complex breakaway points in this state, which means that the characteristic equation of the damping loop has a pair of complex identical roots. Herein, we can obtain a relationship between ω_d and ξ_d through solving the characteristic equation of the damping loop $1 - G_d \cdot (G + d) = 0$. Applying the RRC controller shown in Fig. 2 into this equation, we have

$$1 - \frac{d\left(s^2 + 2\xi_n\omega_n s + \omega_z^2\right)}{s^2 + 2\xi_n\omega_n s + \omega_n^2} \cdot \frac{k_d}{s^2 + 2\xi_d\omega_d s + \omega_d^2} = 0 \quad (5)$$

where $\omega_z^2 = \sigma^2/d + \omega_n^2$ represents the induced zeros by the feedthrough term. Rearranging (5), the characteristic equation will be of the following form as:

$$P(s) = s^4 + K_3 \cdot s^3 + K_2 \cdot s^2 + K_1 \cdot s + K_0 \quad (6)$$

with

$$\begin{cases} K_3 = 2\xi_d\omega_d + 2\xi_n\omega_n \\ K_2 = \omega_d^2 + 2\xi_d\omega_d \cdot 2\xi_n\omega_n + \omega_n^2 - d \cdot k_d \\ K_1 = \omega_d^2 \cdot 2\xi_n\omega_n + 2\xi_d\omega_d \cdot \omega_n^2 - d \cdot k_d \cdot 2\xi_n\omega_n \\ K_0 = \omega_d^2 \cdot \omega_n^2 - d \cdot k_d \cdot \omega_z^2. \end{cases}$$

For the damped system with a pair of complex identical roots in the left half-plane as Fig. 3(b) describes, its characteristic equation should have the following form as:

$$\begin{aligned} P^*(s) &= (s^2 + \alpha \cdot s + \beta)^2 \\ &= s^4 + 2\alpha \cdot s^3 + (\alpha^2 + 2\beta)s^2 + 2\alpha\beta \cdot + \beta^2 \end{aligned} \quad (7)$$

where $\alpha < 0$ and $\Delta = \alpha^2 - 4\beta < 0$ for a repeated pair of complex roots.

Let $P(s) = P^*(s)$ and solve the equation set, an analytical relationship between the parameters in damping controller can be obtained as

$$\begin{aligned} &F_1(k_d, \xi_d, \omega_d) \\ &= \omega_d^2 + 2\xi_d\omega_d \cdot 2\xi_n\omega_n + \omega_n^2 - (\xi_d\omega_d + \xi_n\omega_n)^2 \\ &\quad - \left(\omega_d^2 \cdot 2\xi_n\omega_n + \omega_n^2 \cdot 2\xi_d\omega_d \right. \\ &\quad \left. - d \cdot k_d \cdot 2\xi_n\omega_n\right)/(\xi_d\omega_d + \xi_n\omega_n) - d \cdot k_d = 0 \end{aligned} \quad (8)$$

and

$$\begin{aligned} &F_2(k_d, \xi_d, \omega_d) \\ &= \omega_d^2 \cdot \omega_n^2 - d \cdot k_d \cdot \omega_z^2 \\ &\quad - \left(\omega_d^2 \cdot 2\xi_n\omega_n + \omega_n^2 \cdot 2\xi_d\omega_d - d \cdot k_d \cdot 2\xi_n\omega_n\right)^2 \\ &\quad /(\xi_d\omega_d + \xi_n\omega_n)^2 = 0. \end{aligned} \quad (9)$$

Two implicit functions F_1 and F_2 with respect to k_d, ω_d, and ξ_d can be obtained when solving for breakaway points occurred in the critical state shown in Fig. 3(b). By solving (8) and (9) for a further step, we can obtain the analytical relationship between ω_d and ξ_d, which will lead the system to critical state as shown in Fig. 3(b).

Remark 1: To determine a specific set of the two parameters of ω_d and ξ_d, a tradeoff between the bandwidth and the achievable maximum damping ratio of the damping loop

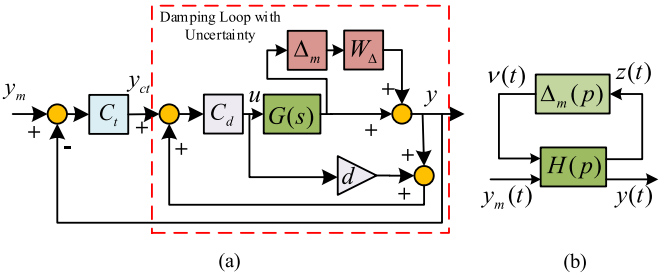

Fig. 4. RRC with multiplicative uncertainty. (a) Closed-loop scheme. (b) Augmented system.

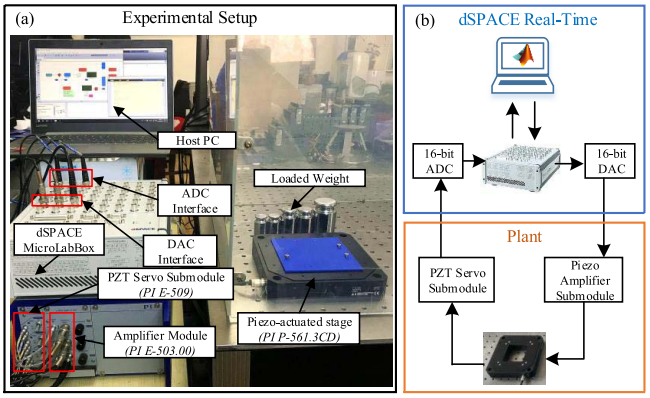

Fig. 5. Experimental setup of the piezoactuated nanopositioning stage. (a) Experimental platform. (b) Block diagram of the signal flow.

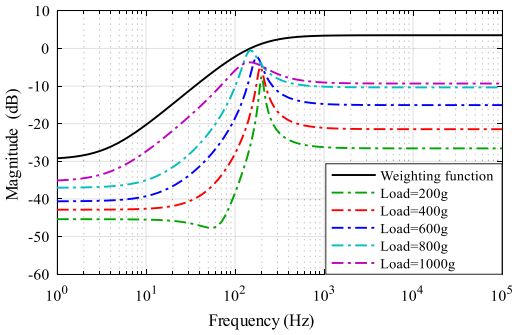

Fig. 6. Multiplicative system uncertainty with load variations and the designed weighting function.

should be made. For this, a discussion is presented in the case studies in Section V.

B. Damping Controller Gain Tuning

In a conventional IRC design, the controller gain is tuned to achieve the maximum damping ratio as stated before. However, the system uncertainty is not taken into consideration in the design process. In the proposed RRC design, we propose to determine the damping controller gain considering two conditions, that is: 1) damping condition as described in (3) and 2) robustness condition based on the small-gain theory.

Theorem 1: The closed-loop system under RRC control with multiplicative uncertainty shown in Fig. 4(a) is internally stable for all uncertainty $\|\Delta_m(s)\| \leq 1$ if and only if

$$\left\| \frac{C_d \cdot G}{1 - C_d \cdot (G + d)} \cdot W_\Delta \right\| < 1 \tag{10}$$

where W_Δ is the weighting function of the uncertainty, which is designed to surpass the measured uncertainty as

$$\|\Delta_m(s) \cdot W_\Delta\| > \|\Delta(s)\| \tag{11}$$

for all frequencies. $\Delta(s)$ is the multiplicative uncertainty that can be obtained by measuring the perturbed system under different loaded masses and calculated by (13).

Remark 2: By performing an upper linear fractional transformation and converting the system in Fig. 4(a) into an augmented format as shown in Fig. 4(b), then Theorem 1 can be derived based on the small-gain theory as described in [21, Ch. 9].

Hereto, the damping controller gain in the proposed RRC can be determined based on the damping condition as well as the robustness condition in (10).

C. Tracking Controller Gain Tuning

As displayed in Fig. 2, the inner damping loop can only alleviate the resonant vibrations caused by the lightly damped modes. A tracking controller in the outer loop needs to be utilized to deal with the hysteresis and the creep nonlinearity to decrease the tracking errors. Considering the ease of calculation and implementation, a high-gain feedback integral is adopted in the outer loop of the proposed RRC, which is also a widely used approach in [5], [13], [17], [19], and [20].

With respect to the tracking controller gain tuning, a graphical method is introduced in [5], for the determination of the proportional–integral control gains. In the RRC design, the maximum allowable overshoot and the settling time of the step response of the closed-loop system are given first. The tracking controller gain is tuned by the trial-and-error method as well as the graphical method to check that the simulated responses agree with the desired performance.

D. Overall Procedure

The overall procedure for the RRC design can be summarized in the following steps.

Step 1: Perform a set of system identifications with a set of load variations (including no loading as the nominal system) and obtain a transfer function model for the nominal system as expressed in (1) as well as a set of systems with perturbation (see Figs. 5 and 6).

Step 2: Calculate the feed-through term d according to (3) to add a pair of resonant zeros followed by the natural poles of the controlled plant as shown in Fig. 3.

Step 3: Plot the state figure for the damping loop based on (8) and (9) to find the proper range for ω_d and ξ_d to lead the system to an ordered state as displayed in Fig. 3(a). The state figure may refer to Fig. 7 in Section V. Determine a candidate range of ω_d and ξ_d based on achieved bandwidth of the damping loop.

Step 4: Plot the figure of achievable maximum damping ratio versus ω_d and ξ_d (see Fig. 8). The solid boundary stands for the values of ω_d and ξ_d to lead the system to a critical

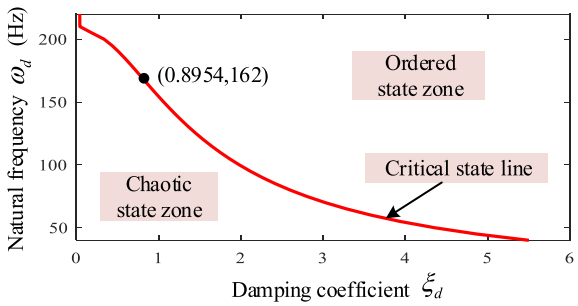

Fig. 7. Range of ω_d and ξ_d for three states in Fig. 3 of the piezoactuated nanopositioner with RRC controller.

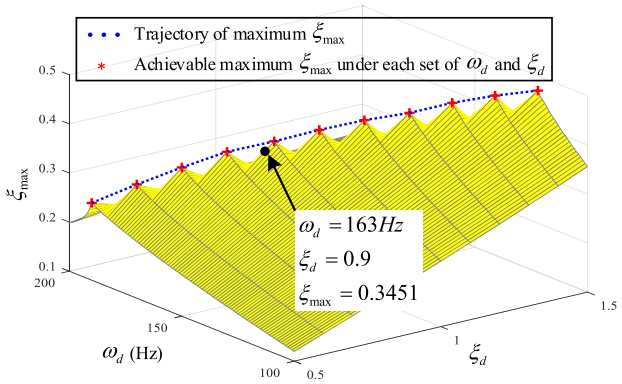

Fig. 8. Achievable maximum damping ratio for the resonant mode versus each set of ω_d and ξ_d.

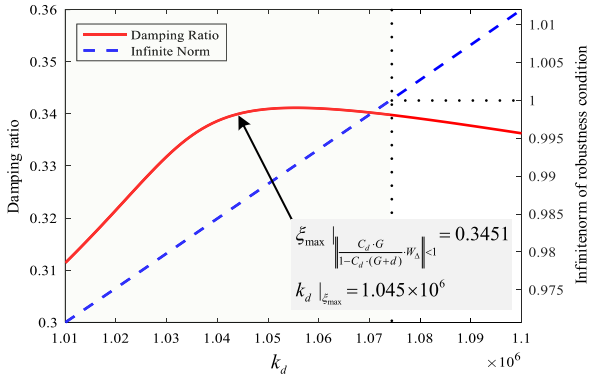

Fig. 9. Determination of damping controller gain k_d based on the damping condition and the robustness condition.

state. Make a tradeoff between the achievable bandwidth and maximum damping ratio and determine a set of ω_d and ξ_d.

Step 5: Calculate the multiplicative uncertainty G_Δ and design the weighting function W_Δ. Tune the damping controller gain k_d to satisfy the damping condition and the robustness condition in (10) (see Fig. 9).

Step 6: Tune the tracking controller gain k_t based on the trial-and-error method to achieve the desired step response performances.

IV. Experimental Setup and System Identification

A. Experimental Setup

The designed controller is implemented on a three-axis piezoactuated nanopositioning stage (model P-561.3CD from Physik Instrumente) as shown in Fig. 5. The terminal motion produced by the actuator is within 0–100 μm for each individual axis. The control input voltage (0–10 V) for each axis is produced by 16-bit digital-to-analog interfaces of the data output module in dSPACE MicroLabBox and subsequently amplified via a piezoamplifier module (model E-503.00 from Physik Instrumente) with a fixed gain of 10 to provide excitation voltage (0–100 V). The displacement of the output is measured via a piezoelectric transducer servo submodule (model E-509.C3A from Physik Instrumente) and is passed to the data input module in dSPACE MicroLabBox with 16-bit analog-to-digital interfaces. Details about the signal flow are shown in Fig. 5(b). The control algorithm is designed in MATLAB/Simulink block diagram on the host PC and then downloaded and executed on the target dSPACE MicroLabBox in the real-time software environment of dSPACE ControlDesk.

In this brief, only the y-axis was used to implement the proposed controller and the sampling frequency of the system was set to 10 kHz.

B. System Identification

1) Nominal Model: A linear model of the y-axis was obtained by applying a step voltage at 10 V into the electrode and recording the corresponding sensor output. Then, the system identification toolbox in MATLAB was used to identify the dynamic model. The obtained continuous transfer function of the dominant dynamics is displayed in (12) with the frequency response described in Fig. 10(a). The first resonant mode of the system with no load occurs at the frequency of 205 Hz with a magnitude of 18.5 dB, where the damping controller is to be designed to reject the unexpected vibrations

$$G(s) = \frac{y(s)}{u(s)} = \frac{1.198 \times 10^6}{s^2 + 110s + 1.673 \times 10^6} \tag{12}$$

where $y[\mu m]$ is the output displacement and $u[V]$ is the driving voltage.

2) Perturbed Model: A set of system identifications was conducted to obtain perturbed models under different loaded masses. Identified system models with load variations are displayed in Fig. 10(a). Corresponding multiplicative uncertainties, shown in Fig. 6, are calculated by

$$\Delta(s) = G_p(s)/G(s) - 1 \tag{13}$$

where $G(s)$ is the identified nominal model in (12), and $G_p(s)$ is the perturbed model with load variations. The weighting function, which is also presented in Fig. 6, is designed as

$$W_\Delta(s) = \frac{s + 23.15}{0.6683s + 691.2}. \tag{14}$$

V. Evaluations and Discussions

In this section, the conventional IRC, PPF, and the proposed RRC are designed on the basis of identified dynamics of the

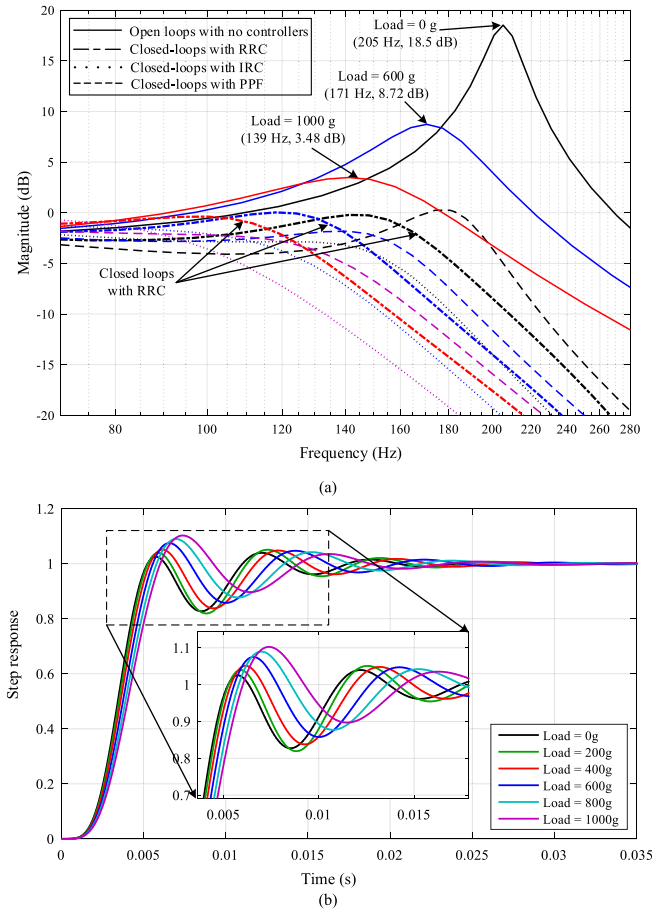

Fig. 10. Comparative results of open loops and closed loops with PPF, IRC, and RRC. (a) System bode diagrams at 0, 600, and 1000 g. (b) Simulation results of step responses with RRC from 0–1000 g.

piezoactuated nanopositioner. Extensive comparisons between these controllers are conducted through tracking experiments, where 5-, 10-, and 20-Hz triangular scanning signals are used as inputs. In addition, the robustness against load variations is verified under a set of loaded masses including 200-, 400-, 600-, 800-, and 1000-g mass.

A. PPF, IRC, and RRC Design

To make fair comparisons, the rise time and the overshoot of step responses of the closed-loop systems are set less than 8 ms and 3% for each control scheme. The damping controller in each scheme is chosen to achieve the maximum damping ratio for the resonant mode, while in RRC design, an additional robustness condition is considered. The tracking controller in each scheme is designed to obtain the desired performance mentioned above.

1) PPF Controller: Utilizing the pole placement approach introduced in [16], designed poles are chosen through shifting 1000 units of poles in (12) along with the real axis in the complex plane. The PPF controller is obtained as

$$C_d^{\text{PPF}} = \frac{4.187 \times 10^6}{s^2 + 6519s + 7.628 \times 10^6}, \quad C_t^{\text{PPF}} = \frac{250}{s}.$$

TABLE I
FREQUENCY- AND TIME-DOMAIN INDEXES

Index	PPF	IRC	RRC
Bandwidth (Hz)	67	135	176
Margin gain (dB)	2.01	2.45	2.02
Margin phase (°)	78.27	68.64	73.40
Rise time (ms)	6.71	3.37	2.86
Overshoot (%)	2.95	1.52	1.68
Damping ratio	0.221	0.268	0.345

2) IRC Controller: According to (3) and (4), the conventional IRC is designed as

$$d = -1.43, \quad C_d^{\text{IRC}} = \frac{1098}{s}, \quad C_t^{\text{IRC}} = \frac{258}{s}.$$

3) RRC Controller: In the proposed RRC, the first step is to determine the proper range of ω_d and ξ_d such that the root locus of the damping loop can follow the trajectory like an ordered state in Fig. 3(a). As the first resonance of the plant occurs at 205 Hz, we can assign a range for ω_d between 40 and 220 Hz, and the corresponding values of ξ_d can be obtained by (8) and (9). As depicted in Fig. 8, the black solid line shows results obtained by (8) and (9), which will lead the damping loop to the critical state. Parameters in the upper area are the proper range for ω_d and ξ_d in RRC. To determine the specific set of parameters, the achievable maximum damping ratio versus parameters are plotted in Fig. 8. It is found that the maximum achievable $\xi_{\max}$ occurs when ω_d and ξ_d are chosen in the critical state line in Fig. 7, which is the same as the blue dotted line in Fig. 8. Therefore, we should choose ω_d and ξ_d in the upper right neighborhood of the critical state line in Fig. 7. A tradeoff between the closed-loop bandwidth and the damping ratio should be made according to the tendency of the critical state line. In this experiment, designed values are $\omega_d = 163$ Hz and $\xi_d = 0.9$, and the achievable maximum damping ratio is $\xi_{\max} = 0.3451$, which is superior to the IRC case as shown in Table I.

According to damping and robustness conditions, the damping controller gain can be determined as $k_d = 1.045 \times 10^6$, as shown in Fig. 9. Hereto, the designed RRC is

$$C_d^{\text{RRC}} = \frac{1.045 \times 10^6}{s^2 + 1840s + 1.044 \times 10^6}, \quad C_t^{\text{RRC}} = \frac{570}{s}.$$

B. Simulation Results

Before conducting experiments, comparisons of closed-loop bandwidth, damping ratio, as well as robustness among three controllers (i.e., PPF, IRC, and RRC) were performed through simulations based on identified nominal and perturbed models. Some performance indexes in both time and frequency domains of closed-loop systems with three controllers are shown in Table I. It can be found that all three controllers satisfy step response requirements set in Section V-A. In addition, all margin gains are larger than 2 dB and margin phases are larger than 30°, which implies that three designed controllers also meet basic margin conditions. Nevertheless, among these

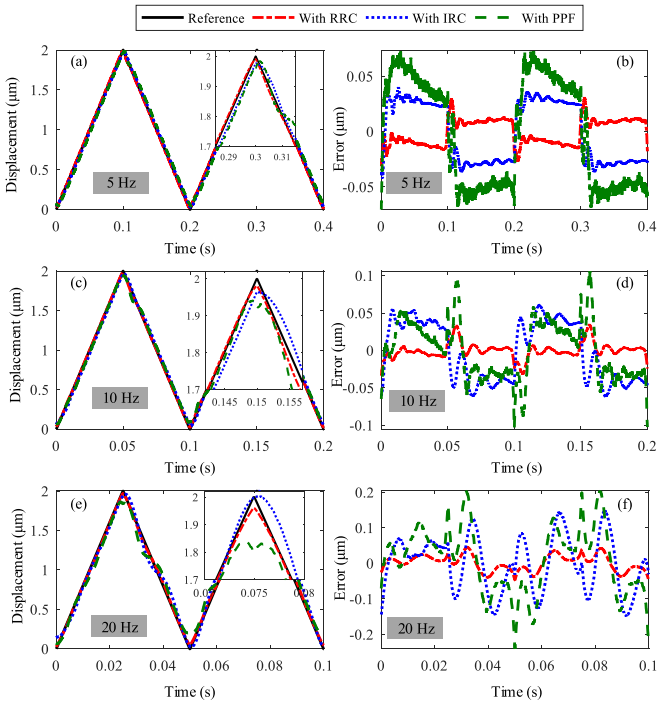

Fig. 11. Experimental results of outputs and tracking errors of raster references. (a)–(b) 5 Hz. (c)–(d) 10 Hz. (e)–(f) 20 Hz.

three controllers, the proposed RRC can obtain the maximum bandwidth of 176 Hz as well as the maximum damping ratio of 0.345 for the resonant mode.

In order to compare the robustness performance under load variations, system bode diagrams and step responses are presented in Fig. 10. It can be clearly seen in Fig. 10(a) that the proposed RRC can guarantee more smooth frequency responses around the changed resonances due to load variations compared with IRC as well as PPF. Regarding step responses under different loads, it can be observed from Fig. 10(b) that the RRC can perform steadily and consistently with load uncertainties within 1000 g.

C. Experimental Results of Raster Tracking

To evaluate the tracking performance of three controllers, a set of raster scanning signals at 5, 10, and 20 Hz are fed into the platform. To evaluate and compare the performance directly using these three controllers, the feedback delay is identified and removed before quantitative analysis. For detailed descriptions about the processing of the delay, readers can refer to (2) in [23].

Tracking results of 0-g load under PPF, IRC, and RRC are recorded in Fig. 11 and Table II. It can be seen that for 0-g load, all three controllers can track raster signals well at 5 and 10 Hz with the root-mean-square error (RMSE) value less than 0.015 μm, which accounts for less than 1% of the positioning stroke of 2 μm. For the 20-Hz case, the RMSE value with PPF and IRC is 0.051 and 0.038 μm, whereas the RMSE with RRC is 0.019 μm, which makes 63% and 50% improvements over PPF and IRC, respectively. The main reason for this is the achieved closed-loop bandwidth of RRC

TABLE II
PERFORMANCE MEASURE

Reference frequency (Hz)	Load (g)	RMSE with PPF (μm)	RMSE with IRC (μm)	RMSE with RRC (μm)
5	0	0.014	0.009	0.005
5	600	0.012	0.010	0.015
5	1000	0.022	0.015	0.014
10	0	0.021	0.025	0.010
10	600	0.045	0.047	0.020
10	1000	0.065	0.051	0.030
20	0	0.051	0.038	0.019
20	600	0.084	0.080	0.023
20	1000	0.128	0.099	0.033

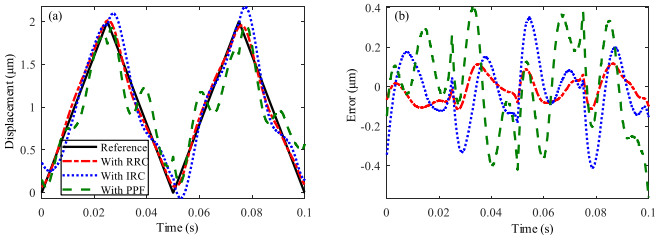

Fig. 12. Tracking results of 20-Hz triangular scanning signals for the system loaded with 1000 g mass.

control is 176 HZ, which is the maximum one among the controller set as presented in Table I.

D. Experimental Results of Robustness Test

As displayed in Fig. 10(a), the worst situation with load variations is 1000 g, where the first resonance is shifted from 205 to 139 Hz. Therefore, in this section, the 20-Hz triangular scanning signals are fed into the closed-loop system under PPF, IRC, and RRC control to test the robustness of three controllers. Simulated bode diagrams of the closed-loop systems are displayed in Fig. 10(a), and the time-domain tracking results are depicted in Fig. 12. In Fig. 10(a), it can be found that the closed-loop system with RRC provides a flatter response compared with PPF and IRC, which is also proved by the tracking error results in Fig. 12. To be more specific, RMSEs of PPF and IRC are 0.128 and 0.099 μm, while the RMSE with RRC is only 0.033 μm (74% less than PPF and 67% less than IRC).

E. Discussions

More specific comparisons of tracking performance among PPF, IRC, and RRC are recorded in Table II. Taking a closer look into the time-domain RMSE, it can be seen that the proposed RRC performs better than PPF and IRC against load variations with a range of 0–1000 g in the experiments. In the aforementioned experiments, triangular signals with a maximum frequency of 20 Hz are utilized, which is approximately ten times lower than the first resonance of the open-loop dynamics. However, it is relatively a high working bandwidth for triangular signals, because they contain all odd harmonics of the basic frequency [7], [16]–[18], which are several times higher than 20 Hz in this case.

It should be noted that both IRC and RRC can deal with vibrational damping of collocated systems that contain multiple dominating resonant modes with only one controller, whereas each resonant mode needs to be damped by an individual damping controller when utilizing PPF approach [19]. Moreover, the PPF scheme always needs a nonlinear search for parameters' tuning, which is more complicated than the analytical approach used in IRC and RRC designs. It is also noteworthy that the proposed RRC scheme can provide a better performance of robustness than conventional IRC, but the design process is a bit more complex as there are more parameters in the controller. Herein, for a system with already known load variations, such as applications in microassembling, cell manipulation, and scanning probe microscope scanning, where consistent positioning performance under different loads are demanded, the proposed RRC can be considered as an alternative option for better robustness.

VI. Conclusion

This brief presents a new RRC scheme for damping control of piezoactuated nanopositioners. The RRC is applied in the inner damping loop to damp resonant-vibrational modes. In the outer loop, a high-gain integral tracking controller is utilized to decrease tracking errors. Parameters of the damping loop are determined through an analytical approach, and controller gains are tuned via a graphic method. The overall design procedure is given for designers. Finally, the developed RRC is applied to a piezoactuated nanopositioner to damp the resonant mode and to compare with the conventional PPF and IRC schemes by tracking raster scanning signals at different frequencies under load variations. Experimental results demonstrate the superiority of the proposed RRC controller.

References

[1] M. Rakotondrabe and I. A. Ivan, "Development and dynamic modeling of a new hybrid thermopiezoelectric microactuator," *IEEE Trans. Robot.*, vol. 26, no. 6, pp. 1077–1085, Dec. 2010.

[2] O. T. Ghalehbeygi, A. G. Wills, B. S. Routley, and A. J. Fleming, "Gradient-based optimization for efficient exposure planning in maskless lithography," *J. Micro Nanolithogr. MEMS, MOEMS*, vol. 16, no. 3, p. 033507, Sep. 2017.

[3] P. Wang and Q. Xu, "Design and testing of a flexure-based constant-force stage for biological cell micromanipulation," *IEEE Trans. Autom. Sci. Eng.*, vol. 15, no. 3, pp. 1114–1126, Jul. 2018.

[4] Q. Xu, "Precision motion control of piezoelectric nanopositioning stage with chattering-free adaptive sliding mode control," *IEEE Trans. Autom. Sci. Eng.*, vol. 14, no. 1, pp. 238–248, Jan. 2017.

[5] C. X. Li, Y. Ding, G.-Y. Gu, and L.-M. Zhu, "Damping control of piezo-actuated nanopositioning stages with recursive delayed position feedback," *IEEE/ASME Trans. Mechatronics*, vol. 22, no. 2, pp. 855–864, Apr. 2017.

[6] J. Ling, Z. Feng, M. Ming, and X. H. Xiao, "Damping controller design for nanopositioners: A hybrid reference model matching and virtual reference feedback tuning approach," *Int. J. Precis. Eng. Man.*, vol. 19, no. 1, pp. 13–22, Jan. 2018.

[7] M. S. Rana, H. R. Pota, and I. R. Petersen, "A survey of methods used to control piezoelectric tube scanners in high–speed AFM imaging," *Asian J. Control*, vol. 20, no. 4, pp. 1379–1399, Jul. 2018.

[8] M. Rakotondrabe, "Multivariable classical Prandtl–Ishlinskii hysteresis modeling and compensation and sensorless control of a nonlinear 2-dof piezoactuator," *Nonlinear Dyn.*, vol. 89, no. 1, pp. 481–499, Jul. 2017.

[9] O. Aljanaideh and M. Rakotondrabe, "Observer and robust H_∞ control a 2-DOF piezoelectric actuator equipped with self-measurement," *IEEE Robot. Autom. Lett.*, vol. 3, no. 2, pp. 1080–1087, Apr. 2018.

[10] J. A. Escareno, M. Rakotondrabe, and D. Habineza, "Backstepping-based robust-adaptive control of a nonlinear 2-DOF piezoactuator," *Control Eng. Pract.*, vol. 41, pp. 57–71, Aug. 2015.

[11] H. Habibullah, H. R. Pota, and I. R. Petersen, "A novel control approach for high-precision positioning of a piezoelectric tube scanner," *IEEE Trans. Autom. Sci. Eng.*, vol. 14, no. 1, pp. 325–336, Jan. 2017.

[12] K. Verbaan, S. san der Meulen, and M. Steinbuch, "Broadband damping of high-precision motion stages," *Mechatronics*, vol. 41, pp. 1–16, Feb. 2017.

[13] A. A. Eielsen, M. Vagia, J. T. Gravdahl, and K. Y. Pettersen, "Damping and tracking control schemes for nanopositioning," *IEEE/ASME Trans. Mechatronics*, vol. 19, no. 2, pp. 432–444, Apr. 2014.

[14] I. R. Petersen and A. Lanzon, "Feedback control of negative-imaginary systems," *IEEE Control Syst. Mag.*, vol. 30, no. 5, pp. 54–72, Oct. 2010.

[15] I. R. Petersen, "Negative imaginary systems theory and applications," *Annu. Rev. Control*, vol. 42, pp. 309–318, Sep. 2016.

[16] S. S. Aphale, B. Bhikkaji, and S. R. Moheimani, "Minimizing scanning errors in piezoelectric stack-actuated nanopositioning platforms," *IEEE Trans. Nanotechnol.*, vol. 7, no. 1, pp. 79–90, Jan. 2008.

[17] D. Russell, A. J. Fleming, and S. S. Aphale, "Simultaneous optimization of damping and tracking controller parameters via selective pole placement for enhanced positioning bandwidth of nanopositioners," *ASME J. Dyn. Syst. Meas. Control*, vol. 137, no. 10, Jul. 2015, Art. no. 101004.

[18] S. K. Das, H. R. Pota, and I. R. Petersen, "Resonant controller design for a piezoelectric tube scanner: A mixed negative-imaginary and small-gain approach," *IEEE Trans. Control Syst. Technol.*, vol. 22, no. 5, pp. 1899–1906, Sep. 2014.

[19] S. S. Aphale, A. J. Fleming, and S. R. Moheimani, "Integral resonant control of collocated smart structures," *Smart. Mater. Struct.*, vol. 16, no. 2, pp. 439–446, Feb. 2007.

[20] M. Namavar, A. J. Fleming, M. Aleyaasin, K. Nakkeeran, and S. S. Aphale, "An analytical approach to integral resonant control of second-order systems," *IEEE/ASME Trans. Mechatronics*, vol. 19, no. 2, pp. 651–659, Apr. 2014.

[21] K. M. Zhou, J. C. Doyle, and K. Glove, "Modeling uncertainty and robustness," in *Robust and Optimal Control*. Englewood Cliffs, NJ, USA: Prentice-Hall, 1996, ch. 9, sec. 2, pp. 211–214.

[22] S. Skogestad and I. Postlethwaite, "Classical feedback control," in *Multivariable Feedback Control: Analysis and Design*, 2nd ed. New York, NY, USA: Wiley, 2007, ch. 2, sec. 4, pp. 34–37.

[23] J. A. Butterworth, L. Y. Pao, and D. Y. Abramovitch, "A comparison of ILC architectures for nanopositioners with applications to AFM raster tracking," in *Proc. Amer. Control Conf.*, San Francisco, CA, USA, 2011, pp. 2266–2271.